A shock tube laser schlieren study of the pyrolysis of isopropyl nitrate

Mark E. Fuller and C. Franklin Goldsmith[*]

School of Engineering, Brown University, Providence, RI, USA

E-mail: franklin_goldsmith@brown.edu

1

Abstract

The decomposition of isopropyl nitrate was measured behind incident shock waves using laser schlieren densitometry in a diaphragmless shock tube. Experiments were conducted over the range of 700 - 1000 K and at pressures of 71, 126, and 240 Torr. Electronic structure theory and RRKM Master Equation methods were used to predict the decomposition kinetics. RRKM/ME parameters were optimized against the experimental data to provide an accurate prediction over a broader range of conditions. The initial decomposition $\mathrm{i-C_3H_7ONO_2 \rightleftharpoons i-C_3H_7O + NO_2}$ has a high-pressure limit rate coefficient of $5.70 \times 10^{22} T^{-1.80} \exp\left[-21287.5/T\right] \ \mathrm{s^{-1}}$. A new chemical kinetic mechanism was developed to model the chemistry after the initial dissociation. A new shock tube module was developed for CANTERA, which allows for arbitrarily large mechanisms in the simulation of laser schlieren experiments. The present work is in excellent agreement with previous experimental studies.

Introduction

Alkyl nitrates or nitrate esters, such as 2-ethylhexyl nitrate (EHN), are used as fuel additives to enhance reactivity and improve the efficiency of combustion engines.[1-6] The reactivity enhancement results from the comparatively weak bond dissociation energy for the nitrate bond, typically between 41-43 kcal/mol.[7-10] Previous experimental work on the chemical kinetics of alkyl nitrates includes shock tubes,[11-13] rapid compression machines,[14-16] flow cells,[17-22] and other techniques.[23-29] These studies, complemented by various theoretical investigations,[7-10,30-34] confirm that thermal decomposition is dominated by the homolytic cleavage of the nitrate bond: $\mathrm{RONO_2 \rightarrow RO + NO_2}$, where RO is an alkyloxy radical (*e.g.* 2-ethylhexyloxy radical in the case of EHN). The subsequent kinetics, particularly with respect to the fuel-bound $\mathrm{NO_2}$ below the thermal $\mathrm{NO_x}$ limit, are less well understood.

In order to develop a more fundamental understanding of alkyl nitrates in low-temperature combustion, the present work focuses on isopropyl nitrate (iPN) as a surrogate for larger

nitrates. The pyrolysis of iPN is measured in a shock tube using the laser schlieren densitometry technique.[35–37] This work is the first part of a broader investigation into nitrate + fuel interactions, including ignition delay times and laminar flame speeds of iPN/propane mixtures.
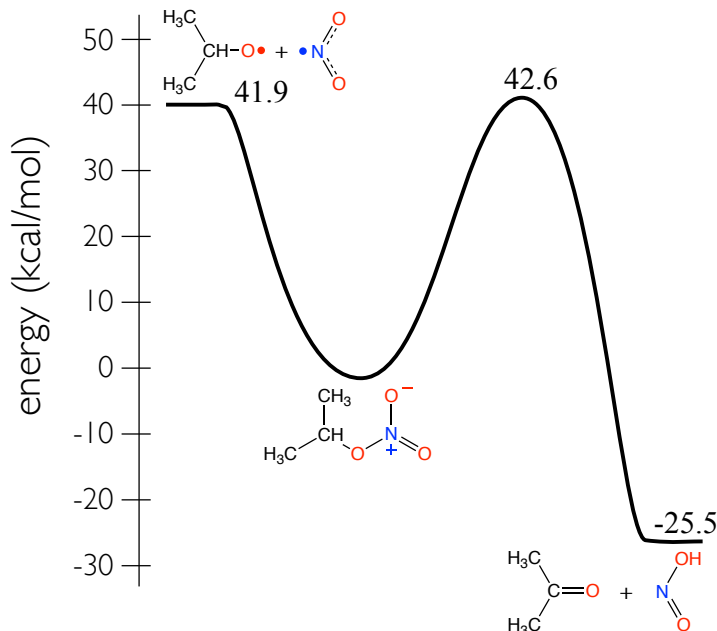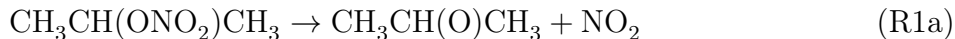

Figure 1: isopropyl nitrate potential energy diagram. The zero-point corrected electronic energies are at the UCCSD(T)-f12a/cc-pVTZ-f12//M11/jun-cc-pVTZ level of theory.

As depicted in Figure 1, isopropyl nitrate has two competing decomposition pathways: $O-NO_2$ homolysis and HONO elimination:

$$CH_3CH(ONO_2)CH_3 \rightarrow CH_3CH(O)CH_3 + NO_2 \tag{R1a}$$

$$\rightarrow CH_3C(O)CH_3 + HONO \tag{R1b}$$

The bond-fission channel, (R1a), is expected to dominate under most conditions. Accordingly, the main product of interest will be the isopropyloxy radical, $CH_3CH(O)CH_3$, which

can undergo one of two beta-scission pathways:

$$CH_3CH(O)CH_3 \rightarrow CH_3CHO + CH_3 \qquad \text{(R2a)}$$

$$\rightarrow CH_3C(O)CH_3 + H \qquad \text{(R2b)}$$

Reaction R2a, which leads to acetaldehyde + methyl radical, is the dominant pathway for the conditions of interest.[20,38]

The decomposition of iPN has previously been measured, but at different conditions and with different diagnostics than in the present work. The earliest work, by Griffiths, Gilligan, and Gray, focused on the use of iPN as a monopropellant. The first of two publications focused on the mechanism of iPN decomposition; the authors measured total pressure in a cell as a function of time and inferred a decomposition rate constant.[25] The second study examined decomposition of iPN at temperatures between 1300 and 1550 K and pressures greater than 14 bar in both closed and flow reactor configurations.[26] These high-pressure and temperature experiments directly examined the suitability of iPN as a monopropellant, with emphasis on determination of the characteristic burning velocity, c^*. Zaslonko et al. used laser absorption spectroscopy in a shock tube to measure the decomposition rate between 700 - 1000 K and pressures between 375 - 750 Torr.[11] Beeley, Griffiths, and Gray used a rapid compression machine with gas-sampling techniques to characterize the kinetics.[14,15] Toland and Simmie performed shock tube studies of smaller alkyl nitrates (n-propyl, isopropyl, n-butyl, isobutyl, isoamoxyl nitrate) and oxygen blends dilute in argon.[12] Toland and Simmie found support for the decomposition given in reaction R1a and also found that branched alkyl nitrates had longer ignition delay times than straight chain species due to the kinetics of isoalkyloxy versus n-alkyloxy radical decomposition. Most recently, Morin and Bedjanian measured the decomposition kinetics via mass spectrometry in a flow cell between 473-658 K

and 1 - 12 Torr.[20]

The present work complements a prior study on the use of alkyl nitrites as radical sources in shock tubes.[39] Randazzo et al. studied the pyrolysis of n-propyl nitrite, n-butyl nitrite, and isobutyl nitrite using laser schlieren densitometry behind the incident shock. Those nitrites undergo a similar $O-NO$ homolysis to yield n-propyloxy, n-butyloxy, and isobutyloxy alkyloxy radicals, which in turn undergo prompt beta-scission to yield CH_2O + ethyl, n-propyl, or isopropyl radicals, respectively. In the present work, iPN produces isopropyloxy and thence methyl radicals.

Experimental

Experiments were conducted with laser-schlieren densitometry (LS) in the Brown Shock Tube (BST),[40] a diaphragmless shock tube facility, conceptually similar to the shock tube of Tranter and coworkers at Argonne National Laboratory.[41,42] The diaphragmless tube replaces the traditional diaphragm that separates the high and low-pressure sections with a piston valve capable of rapid opening times. The piston valve utilizes a metal bellows as the spring in a normally-open, pneumatic valve design. An isolated chamber is backfilled with nitrogen to compress the bellows and isolate the driver and driver sections. The high-pressure driver section is filled to the desired loading pressure, P_4, with helium, and the low-pressure driven section is filled to pressure P_1 with the reactant gas mixture. To fire a shock, the pressure compressing the bellows is dumped into an evacuated tank and the spring force of the bellows opens the piston valve. The diaphragmless shock tube design offers significant improvements in control of post-shock conditions and reductions in turnaround time, but at a cost of a decrease in shock strength for the same loading conditions as compared with the use of diaphragms.

The BST utilizes a software control panel to electronically control valving, which allows for automatic loading of the pre-shock conditions, P_1 and P_4. For each experiment, a turbo-

molecular pump was used to evacuate the driven section down to a pressure less than 1×10^{-4} Torr prior to filling the driven section to the desired P_1. The shock velocity is measured from the time intervals as the shock wave passes a series of six evenly spaced transducers (Dynasen CA-1135) located at the same axial position on the shock tube as the diagnostic. The time intervals are recorded using a transducer readout module (TRM) designed and constructed by Argonne National Laboratory. The post-shock temperature and pressure, P_2 and T_2 are calculated from the shock velocity, u, and initial conditions P_1 and T_1 with an assumption of frozen equilibrium. Based on previous reporting for the same transducers and TRM, the uncertainty in velocity is estimated to be 0.2% and the corresponding error in temperature and pressure to be under 0.5%.[43]

The laser schlieren densitometry diagnostic was developed and originally described by Kiefer and Lutz[44,45] and subsequently documented in great detail by Kiefer and coworkers.[35–37] In LS, the deflection of a laser beam, which is perpendicular to the tube axis and passes through the centerline, is recorded as a function of time and mapped to the density gradient in the shock tube. Calculation of the density gradient,$d\rho/dz$, from deflection angle, θ, is a function of the shock tube width, W, and refractivity of the gas mixture, K_L:

$$\theta = \frac{3}{2} K_L W \frac{d\rho}{dz} \tag{1}$$

where K_L is a weighted average of the molar refractivities of the individual gas species, R_L, their mole fractions, x, and the mixture average molecular weight, $\bar{M}$.

$$K_L = \sum_i R_{L_i} \frac{x_i}{\bar{M}} \tag{2}$$

For each experiment, the LS system is calibrated using a synchronous AC motor with a known period to sweep the beam across a split photodiode detector. The known angular velocity and differential photodiode voltage signal versus time allow for a calibrated map of differential detector signal to laser beam deflection angle. In preparation for each experiment,

the beam is re-centered to zero deflection (zero signal) following the calibration phase. During the course of the experiment, the voltage differential from the split photodiode is recorded and mapped according to the calibration to produce the deflected beam angle as a function of time; this θ is then used in Equation 1 to determine the density gradient.

For these experiments, the molar refractivities of Ar and Kr were taken from Gardiner[46] as 4.198 cm^3 mol^{-1} and 6.367 cm^3 mol^{-1}, respectively. The molar refractivity of isopropyl nitrate is 23.7$\pm$0.3 cm^3 mol^{-1}, as predicted by the PhysChem module of ACD/Labs Percepta Platform software[47] and published on ChemSpider.[48] The refractivity of the gas mixture is assumed to be constant over the course of the experiment due to the dilute reactant composition.

Isopropyl nitrate, 98%, was purchased from Millipore Sigma and was degassed prior to mixture preparation by repeated freeze-pump-thaw cycles with liquid nitrogen. Mixtures of 1% and 2% isopropyl nitrate were prepared dilute in argon, and mixtures of 0.5%, 1%, and 2% isopropyl nitrate were prepared dilute in krypton. All mixtures were prepared manometrically in a 72 L glass flask and were allowed to homogenize overnight (minimum 16 hours) before use. The flask was evacuated to a total pressure less than 1×10^{-4} Torr before mixtures were prepared.

Modeling

Computational kinetics

Stationary points on $C_3H_7NO_3$ potential energy surface, illustrated in Figure 1, were first computed using density functional theory. Geometry optimization and normal mode analysis were performed with the M11/jun-cc-pVTZ functional and basis set.[49] After the lowest energy conformer was identified and optimized, single-point energy calculations were performed using UCCSD(T)-F12a/cc-pVTZ-f12 theory.[50–52]

Microcanonical transition state theory (TST) calculations were performed using the

RRKM/ME code MESS,[53,54] which is part of the computational kinetics package PAPR developed by Argonne National Laboratory.[55] A single exponential was used to model the collisional energy transfer, with an initial value of $\langle\Delta E_{\text{down}}\rangle = 300\,(T/298[\text{K}])^{0.85}$ cm^{-1}. For the bond fission channel to form $CH_3CH(O)CH_3 + NO_2$, an analytic model was used to describe the interaction potential, as implemented using the `PhaseSpaceTheory` keyword in MESS.[56–58] The coefficient of the interaction potential, αr^{-6}, was initially set to $\alpha = 0.1$ (internal units) so that the high-pressure limit of the reverse reaction had a rate coefficient of approximately 2×10^{-11} cm^3/molecule-s, which is a reasonably accurate approximation to the radical $+\ NO_2$ reactions in the high-pressure limit.[39,59] For transition states that have a first-order saddle point in potential energy, standard rigid-rotor harmonic-oscillator models were used to compute the microcanonical rate coefficients. Torsional modes were treated separately, with rotational scans performed in $10°$ increments, and the partition function was computed via summation over the energy levels for the corresponding 1D Schrödinger equation. The phenomenological rate constants were fit to a modified Arrhenius expression for each pressure, and the results were then formatted for use in logarithmic pressure interpolation, or the `PLOG` formalism.

Because two of the main products are NO_2 and CH_3CHO, separate transition state theory calculations were performed for the abstraction of a hydrogen from the methyl group. Abstraction was considered for both the O and N in NO_2: $CH_3CHO + NO_2 \rightarrow CH_2CHO + HONO$, and $CH_3CHO + NO_2 \rightarrow CH_2CHO + HNO_2$, respectively. The compound method used in Ref. 60 and Ref. 61 was applied for the two abstraction reactions. Geometry optimization and normal mode analysis were performed using the B2PLYPD3 functional with the cc-pVTZ basis set.[62–64] Single-point calculations were performed on the optimized geometries at the UCCSD(T)-F12a/cc-pVTZ-f12. All DFT calculations were performed using Gaussian G09;[65] all wavefunction methods were performed using MOLPRO.[66]

Nitro alkanes can undergo a nitro-nitrite isomerization, which has a well-defined saddle point.[67] For alkyl nitrates, in contrast, the analogous reaction is more complicated.

8

Arenas et al. investigated the possibility of isomerization of methyl nitrate, CH_3ONO_2, to methylperoxy nitrite, CH_3OONO, using multireference methods.[34] They concluded that this isomerization reaction cannot occur as a single reaction, but rather must be a two-step process of dissociation followed by recombination. We performed similar calculations for iPN using CASPT2(14e,11o)/cc-pVTZ.[68] Consistent with Ref. 34, we were unable to find a saddle point for the nitro-nitrite rearrangement. Accordingly, we do not include isomerization to isopropylperoxy nitrite in the potential energy surface.

To improve the agreement between the experimental data and the modeling results, select parameters within the RRKM/ME were optimized. First, the $CH_3CH(ONO_2)CH_3 \rightarrow CH_3CH(O)CH_3 + NO_2$ bond dissociation energy (BDE) was varied from the nominal value of 41.9 kcal/mol $\pm$ 2 kcal/mol in 0.25 kcal/mol increments. Second, the pre-factor for the energy transfer parameter, $\langle \Delta E_{down} \rangle$ was varied between 200 and 400 cm^{-1} in 25 cm^{-1} increments. Finally, the interaction potential coefficient, α, was varied between 10^{-3} and 10^1 in 21 logarithmic steps. As a result, 2079 individual RRKM/ME simulations were performed for the same T_2 and P_2 as the experiments. The combination of parameters that minimized the sum of square error between the log of the measured rate constants and the log of the RRKM/ME predictions was chosen as the optimum set. The optimization of electronic structure and master equation properties against experimental data is inspired by the Multiscale Informatics (MSI) of Burke and coworkers.[69–72]

Mechanism development

To model the LS experiments, a new chemical kinetic mechanism was developed. This mechanism combines the present $C_3H_7NO_3$ kinetics with two pre-existing mechanisms. The first mechanism is the forthcoming H/C/O "Theory-Informed Chemical Kinetic Model" of Jim Miller, Stephen Klippenstein, and coworkers, which covers $C_0 - C_3$ chemistry in depth, as well as some larger species that result from $C_3 - C_3$ coupling. The second mechanism is the nitrogen chemistry of Peter Glarborg.[73] The nitrogen chemistry was augmented by the

HONO/HNO$_2$ submechanism of Goldsmith and coworkers.[60,61,74]

Additionally, some reactions relevant for the pyrolysis of nitromethane were taken from Ref. 67. Thermodynamic data for isopropyl nitrate were taken from Ref. 75. The mechanism is formatted for use in CANTERA, which is a suite of tools for problems in reactive flow.[76] The mechanism is available in the Supplementary Material.

Simulation of the density gradient

To model the experiments, a new module was developed in CANTERA, similar to incident shock tube module in CHEMKIN II.[77] The complete derivation of the governing equations, along with the necessary post-processing equations, are provided in the Supplemental Material.

The measured density gradient of the reacting system may be compared to the modeled density gradient, which is related to the kinetics of the gas behind the incident shock:

$$\frac{d\rho}{dz} = \frac{1}{v}\frac{1}{1+\beta}\sum_{k}^{N_{\text{species}}} \dot{\omega}_k W_k \left(\frac{h_k}{\overline{C}_p T} - \frac{\overline{W}}{W_k} \right) \tag{3}$$

$$= \frac{1}{\overline{C}_p T}\frac{1}{v}\frac{1}{1+\beta}\sum_{j}^{N_{\text{rxns}}} r_j \left(\Delta H_j - \overline{C}_p T \overline{W} \Delta N_j \right) \tag{4}$$

where v is the gas velocity behind the incident shock, $\dot{\omega}_k$ is the net rate of production of species k per unit volume, W_k is the molar mass of k, r_j is the net rate of reaction j, $\overline{C}_p$ is the mean heat capacity at constant pressure, and $\overline{W}$ is the mean molecular weight of the mixture. $\beta \equiv v^2 \left(1/\overline{C}_p T - \overline{W}/RT \right)$ is a dimensionless group used in the derivation.

The density gradient is dominated by the rate of heat release (positive or negative) for each reaction. This heat release rate can be expanded in terms of the net rate of reaction for all the species, as in Equation (3), or in terms of individual reactions, Equation (4). In the latter case, we see that the density gradient is directly proportional to the heat of

reaction, ΔH_j, with a (typically minor) correction for the change in the number of moles ΔN_j. Accordingly, the LS diagnostic is blind to mildly endothermic reactions for which $\Delta H_j \approx \overline{C_p T W} \Delta N_j$. At time $t = 0$, the only reactions that matter are the decomposition reactions of the reactant.

The new CANTERA implementation represents a significant advancement in modeling laser schlieren densitometry, since it allows for arbitrarily large and complex chemical kinetic mechanisms to be used. As will be demonstrated below, the signals at longer times show considerable sensitivity to reactions that follow from the primary decomposition kinetics. With the ability to include large, theory-informed chemical kinetic mechanisms, the laser schlieren method provides new validation targets for mechanism development and refinement. Because the technique operates on a different time scale, it is complementary to other, more common diagnostics in combustion. The experimental data, along with the chemical kinetic mechanism and the CANTERA script, are provided as Supplemental Material, so that other research groups can test other mechanisms against these targets.

Results and discussion

Approximately 100 shock tube experiments were conducted with mixtures of isopropyl nitrate dilute in argon or krypton, at concentrations of 0.5%, 1%, and 2%. Experiments were conducted over the range of 700 - 1000 K and at nominal pressures of 71, 126, and 240 Torr. No significant difference was observed in the rate of iPN dissociation between argon and krypton bath gases. A complete listing of shock conditions and the corresponding density gradients are provided as Supplemental Material.

Representative shocks are provided in Figures 2 and 3, along with plots indicating the reactions that contribute at least 5% to the observable density gradients. A list of all the major reactions (those found to have contributed at least 1% to the density gradient in any of the collected shocks) is provided as Table 1.
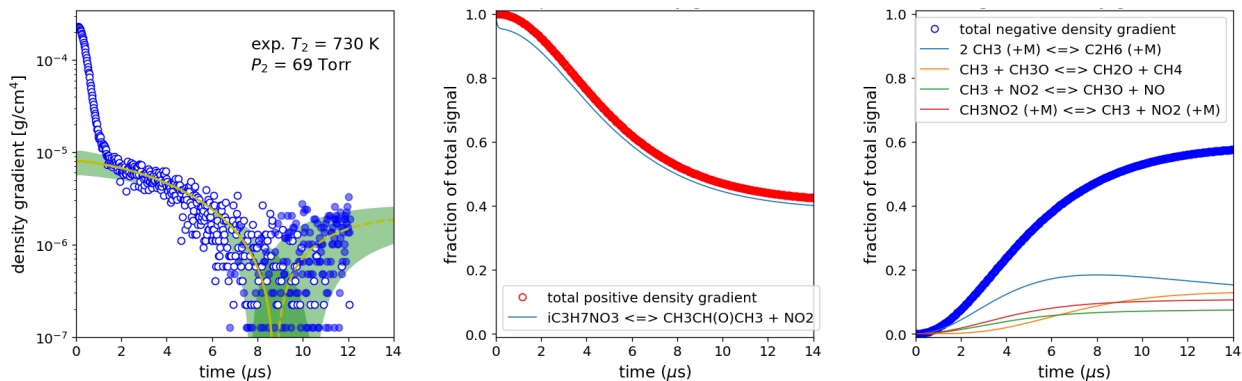
11

Figure 2: Typical lower-temperature shock: $T_2 = 730$ K and $P_2 = 69$ Torr. Under these conditions, the initial dissociation is responsible for the majority of the signal for the first 7 μs. The shaded green region represents an uncertainty band of 30% in the rate coefficient for Reaction (R1a).
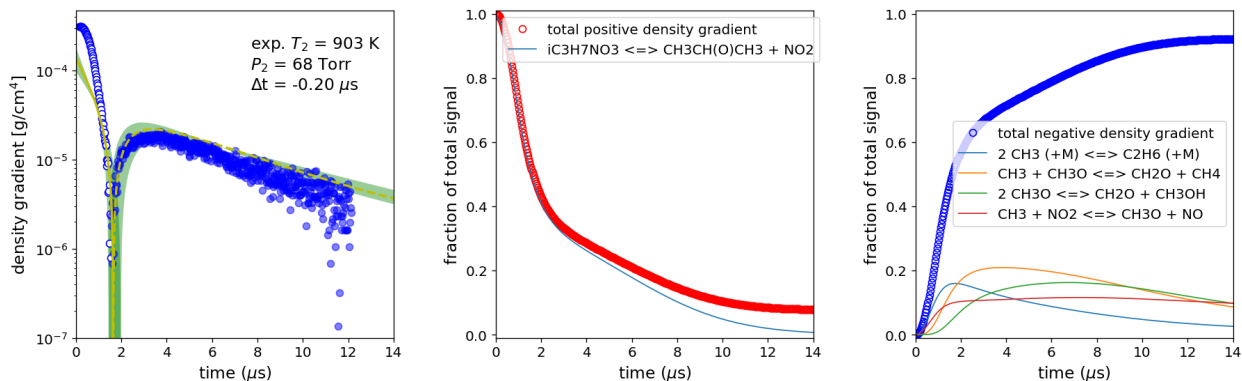

Figure 3: Typical higher-temperature shock: $T_2 = 903$ K and $P_2 = 68$ Torr. Under these conditions, the contribution of the initial dissociation is short, and secondary chemistry dominates after 1 μs. The shaded green region represents an uncertainty band of 30% in the rate coefficient for Reaction (R1a).

The rapid decrease in the value of the experimental density gradient in the first <1 μs in Figure 2 is due to the passing of the shock front and obscures the chemical signal at $t = 0$. Following the passage of the shock front, the remainder of the density gradient is due to the chemistry behind the shock. As indicated by Equation (4), endothermic reactions have a positive contribution to the density gradient, and exothermic reactions have a negative contribution. Because the initial decomposition of iPN is dominated by the bond fission pathway, Reaction R1a, which has a heat of reaction of $\Delta H_{rxn} = 41.9$ kcal/mol, the initial signal after the shock front is always positive. This initial signal, when the majority of the

12

observable density gradient is due to a single reaction, is used to obtain the decomposition rate constant. The rate constant for Reaction R1a was adjusted for each experiment to provide a fit to the early portion of the curve, when the signal-to-noise ratio is high and the signal is dominated by a single reaction. This process is iterated until a final Arrhenius expression satisfactorily models all the experiments at a given pressure. These rate constants, determined on a per-experiment basis, are plotted as individual points in Figure 4. The complete set of experimental data are provided in the Supplemental Material. For the present work, only the rate constant for Reaction R1a was adjusted. No attempt was made to improve the model fit by modifying the rate constants taken from the literature, Table 1.

The middle panes in Figures 2 and 3 plots the fraction of total signal that is due to endothermic reactions, and the right panes plots the fraction of total signal due to exothermic reactions. A common feature in most LS experiments is a change in the sign of the density gradient, *e.g.* at 9 μs in Figure 2 and at 1 μs Figure 3. Because the density gradient is plotted on a logarithmic axis, positive density gradients are represented by open circles and solid lines, and negative density gradients are represented by solid circles and dashed lines. This sign change occurs when the net contribution of exothermic reactions exceeds the net contribution of endothermic reactions – *i.e.* when the blue circles in the right-hand panes become greater than 0.5. This transition can be gradual at lower temperatures, Figure 2, but at higher temperatures, it can be abrupt, Figure 3. At lower temperatures, the majority of the signal is dominated by Reaction R1a. As the post-shock temperature increases, the time at which the density gradient switches from net positive to net negative shifts to earlier times. Eventually, the decomposition is so fast that it is buried beneath the shock front; for temperatures beyond that point, the density gradient is entirely dominated by post-dissociation chemistry.

Also included on the density gradient plots are uncertainty bounds associated with the fitted rate constant for Reaction (R1a). The shaded green area represents the range of possible density gradients if the rate constant for Reaction (R1a) is scaled up or down by up

to 30%. The 30% uncertainty band adequately captures the initial scatter in the measured density gradient immediately after the passage of the shock when the signal is entirely dominated by Reaction (R1a). Conversely, at long reaction times and higher temperatures, $e.g.$ $t \geq 8$ μs in Figure 3, the modeled density gradient is no longer sensitive to the rate constant for Reaction (R1a), and the shaded green region is narrow.

Following the initial dissociation, the next reaction to occur is Reaction R2a, the beta-scission of isopropyloxy to form methyl radicals + acetaldehyde. However, because this reaction is mildly endothermic, $\Delta H_{rxn} = 4.9$ kcal/mol, it has a modest contribution to the LS signal, typically between 1-4%. Nonetheless, this reaction is indirectly important to the overall model fidelity, as the entire exothermic signal depends upon the methyl radicals generated by Reaction R2a. As seen in the right-hand plots in both Figures 2 and 3, the recombination of methyl radicals, Reaction #5 in Table 1, is the most important reaction in the first few μs after the density gradient switches from positive to negative. This reaction competes with $CH_3 + NO_2 \rightarrow CH_3O + NO$, Reaction #19, since these two radicals are formed in a one-to-one ratio following the reaction sequence R1a + R2a. Reaction #19 is important because it leads to the formation of methoxy radicals, which are involved in two disproportionation reactions $CH_3 + CH_3O \rightarrow CH_4 + CH_2O$, Reaction #11, and $CH_3O + CH_3O \rightarrow CH_2O + CH_3OH$, Reaction #13. These four radical-radical reactions each contribute between 10-20% of the total signal at longer observation times. It is worth noting that Reaction #13, according to Tsang's database,[78] is estimated from room-temperature data and has an uncertainty factor of 10; reducing this rate constant within this uncertainty range would improve the agreement between model predictions and measured density gradients. The most important reactions for the post-dissociation chemistry are summarized in Table 1. Collectively, these reactions account for more than 99% of the total signal for all of the experiments.

Table 1: Key reactions contributing to observed density gradients. For pressure-dependent reactions, the high-pressure limit is presented.

Number	Reaction	A^a	n^a	$E_a{}^a$	Ref.
1	i-$C_3H_7NO_3 \rightleftharpoons CH_3CH(O)CH_3 + NO_2$	3.36×10^{42}	-8.02	49160	P.W.
2	i-$C_3H_7NO_3 \rightleftharpoons CH_3C(O)CH_3 + HONO$	7.42×10^{31}	-6.09	47440	P.W.
3	$CH_3CH(O)CH_3 \rightleftharpoons CH_3 + CH_3CHO$	6.42×10^{27}	-4.63	18400	38
4	CH_3O (+M) $\rightleftharpoons CH_2O + H$ (+M)	1.32×10^{16}	-0.588	26772	79,80
5	2 CH_3 (+M) $\rightleftharpoons C_2H_6$ (+M)	8.88×10^{16}	-1.16	775	81
6	$HCO + OH \rightleftharpoons CO + H_2O$	4.61×10^{13}	0.011	-115	79,80
7	$H + HCO \rightleftharpoons CO + H_2$	1.20×10^{14}	0.0	0	79,80
8	C_3H_8 (+M) $\rightleftharpoons C_2H_5 + CH_3$ (+M)	1.55×10^{24}	-2.034	90388	82
9	$CH_2O + OH \rightleftharpoons H_2O + HCO$	7.82×10^{7}	1.63	-1055	83
10	$CH_3O + OH \rightleftharpoons CH_2O + H_2O$	1.81×10^{13}	0.0	0	78
11	$CH_3 + CH_3O \rightleftharpoons CH_2O + CH_4$	2.41×10^{13}	0.0	0	78
12	$CH_3O + HCO \rightleftharpoons CH_3OH + CO$	9.04×10^{13}	0.0	0	78
13	2 $CH_3O \rightleftharpoons CH_2O + CH_3OH$	6.02×10^{13}	0.0	0	78
14	$CH_3CHO + OH \rightleftharpoons CH_2CHO + H_2O$	5.04×10^{13}	0.0	4789	84
15	$CH_3CHO + OH \rightleftharpoons CH_3CO + H_2O$	2.61×10^{12}	0.0	-733	84
16	$HCO + NO \rightleftharpoons CO + HNO$	6.90×10^{12}	0.0	0	85
17	$HCO + NO_2 \rightleftharpoons CO + HONO$	5.00×10^{12}	0.0	0	85
18	$CH_3 + HNO \rightleftharpoons CH_4 + NO$	1.50×10^{11}	0.76	348	86
19	$CH_3 + NO_2 \rightleftharpoons CH_3O + NO$	1.10×10^{13}	0.0	0	87, 88
20	$CH_3O + HNO \rightleftharpoons CH_3OH + NO$	3.20×10^{13}	0.0	0	89
21	$CH_3O + NO \rightleftharpoons CH_2O + HNO$	7.50×10^{12}	0.0	2017	90
21	duplicate	2.50×10^{18}	-2.56	0.0	90
22	$CH_3O + NO_2 \rightleftharpoons CH_2O + HONO$	6.00×10^{12}	0.0	2285	91
23	$CH_2CHO + NO_2 \rightleftharpoons CH_2CO + HONO$	2.00×10^{15}	-0.68	1430	92
24	CH_3NO_2 (+M) $\rightleftharpoons CH_3 + NO_2$ (+M)	1.80×10^{16}	0.0	58500	87, 93
25	$H + NO_2 \rightleftharpoons NO + OH$	2.01×10^{11}	0.84	-1058	74
26	$CH_2CHO + HONO \rightleftharpoons CH_3CHO + NO_2$	2.98×10^{-5}	4.49	6464.2	P.W.
27	$CH_2CHO + HNO_2 \rightleftharpoons CH_3CHO + NO_2$	3.46×10^{-5}	3.84	2049.5	P.W.

^{a} Modified Arrhenius format, $k = A \left(T/T_0\right)^n \exp\left(-E_a/RT\right)$. Units: cm, s, K, mole, calorie. $T_0 = 1$ K.

The optimized RRKM/ME model predictions are included as solid line in Figure 4. As a result of the optimization procedure, the bond dissociation energy decreased from 41.9 to 40.9 kcal/mol. The final collisional energy transfer parameter, $\langle \Delta E_{\text{down}} \rangle$, was reduced from 300 to 250 cm^{-1}. The interaction potential prefactor, α, was increased to 1.78×10^{-1}. The resulting high-pressure limit for the reverse reaction $CH_3CH(O)CH_3 + NO_2 \rightarrow CH_3CH(ONO_2)CH_3$ was $2.76 \times 10^{-13} T^{0.58} \exp\left[272.2/T\right]$ cm^3/molecule-s, which is
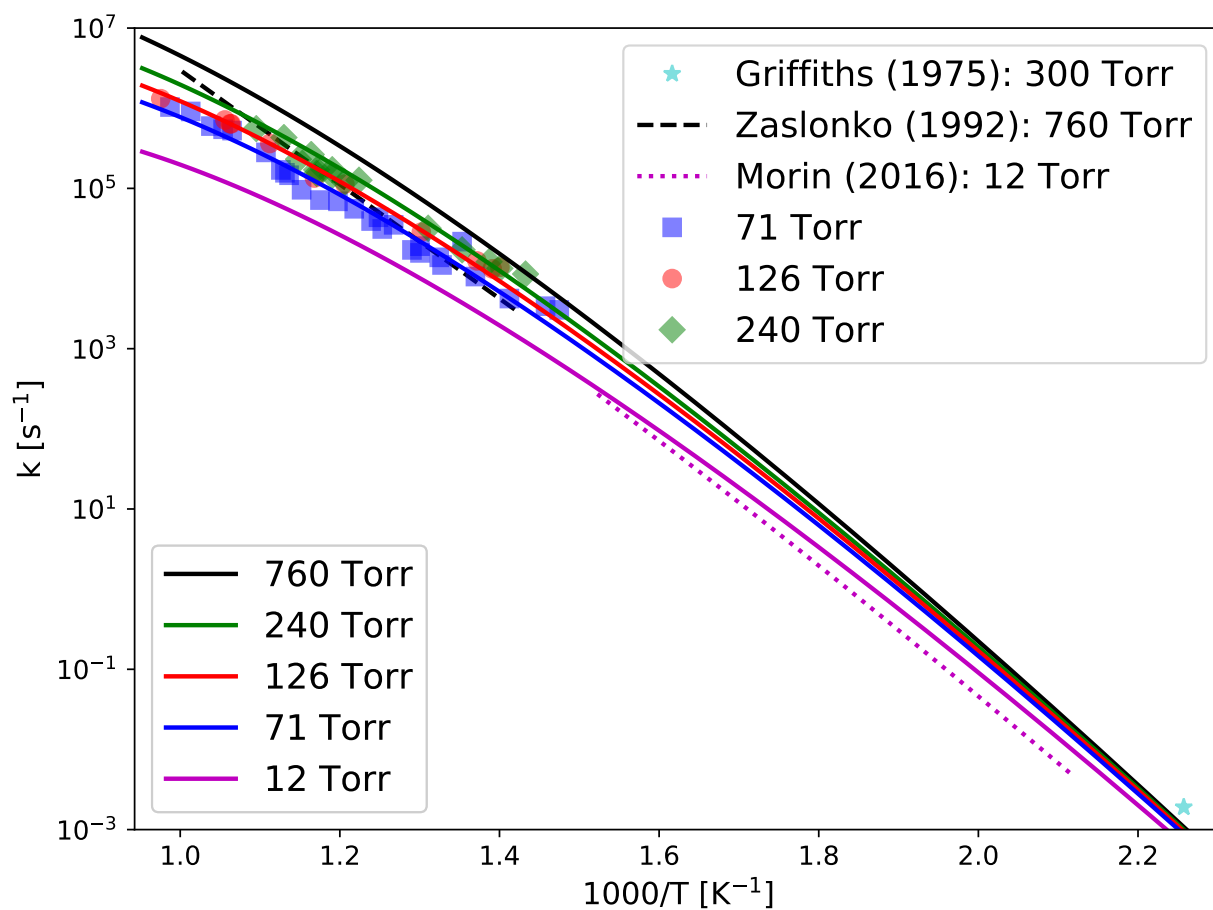
Figure 4: Experimental and model predictions for the decomposition of isopropyl nitrate. The symbols are the LS data. The solid lines are the optimized RRKM/ME predictions at five different pressures. The dashed black line is from Ref. 11, and the dotted magenta line is from 20.

approximately 2×10^{-11} cm^3/molecule-s for the present conditions. These adjustments are well within the expected uncertainty in the computational methods. As can be seen in Figure 4, the agreement between the model and experimental data is excellent. The RRKM/ME predictions agree with a linear regression of the experimental data to an Arrhenius fit to within 20%.

Also included in Figure 4 are three prior literature studies for which rate constants were published, References 25, 11, and 20. Griffiths et al. provided a measurement at only one temperature, 443 K. Neither Zaslonko et al. nor Morin and Bedjanian provided measured rate constants at specific temperatures; instead, they provide Arrhenius fits and Troe forms to their data, respectively. Their recommended rate constants are shown as dashed black and dotted magenta lines, respectively; the model line for Morin and Bedjanian is their Troe expression evaluated at 12 Torr, which was the highest pressure in their system. In general, the agreement between the present work and the prior studies is quite good. Quantitatively, the data from Zaslonko et al., which were taken at a nominal pressures between 375 and 750 Torr, is lower than the present data for 240 Torr and has a slightly higher activation energy. Similarly, the data from Morin and Bedjanian is slightly below the model predictions, but is still well within the extrapolated uncertainty, especially considering the difference in bath gases and detection methods.

Time-shifting

Typical laser-schlieren raw signals have a single positive spike, which is often preceded by a valley. An example of such a signal and the corresponding density gradient, with overlaid model prediction, is provided in Figure 5. In the case of these experiments, the time zero from the reaction, t_0, can be found using the technique established by Kiefer, which typically locates t_0 to within $\pm$ 0.2 μs.[35] Some of the experiments with isopropyl nitrate, however, produced signals which contained multiple peaks or peaks consisting of sections with two slopes, an example of which is provided in Figure 6a. The exact cause of this "double spike"

for iPN is not known, but it is believed to be an artifact of the optical configuration that was used for this system.
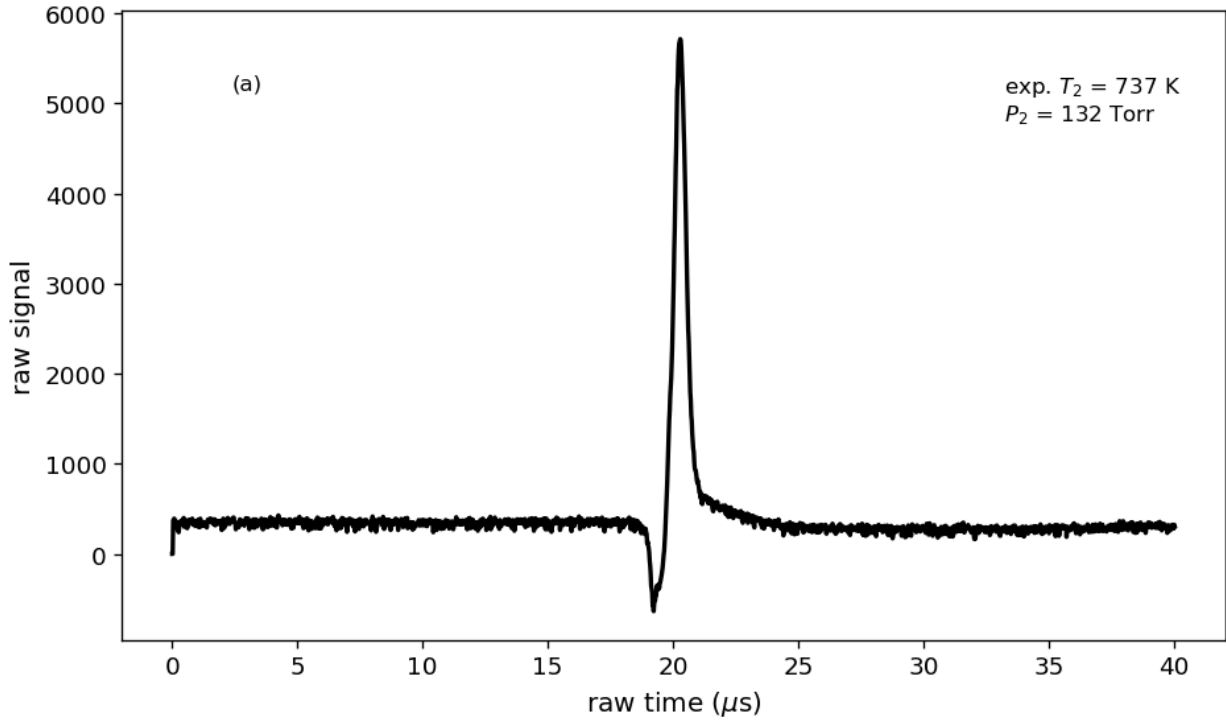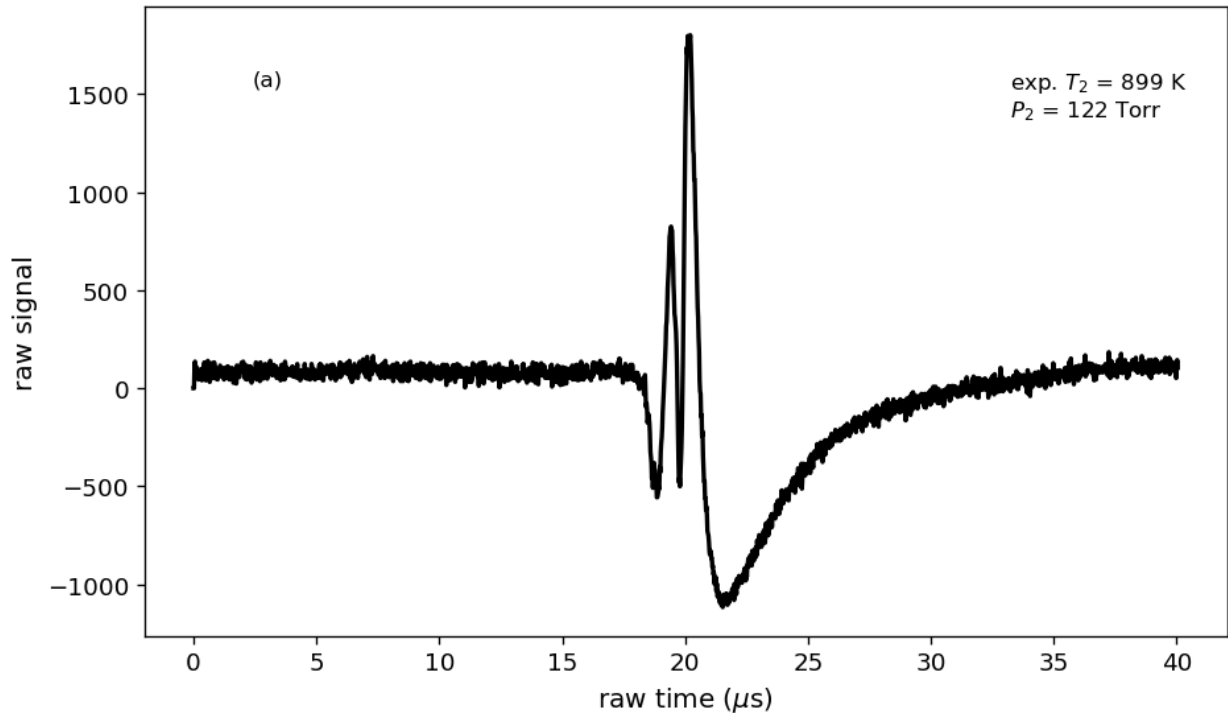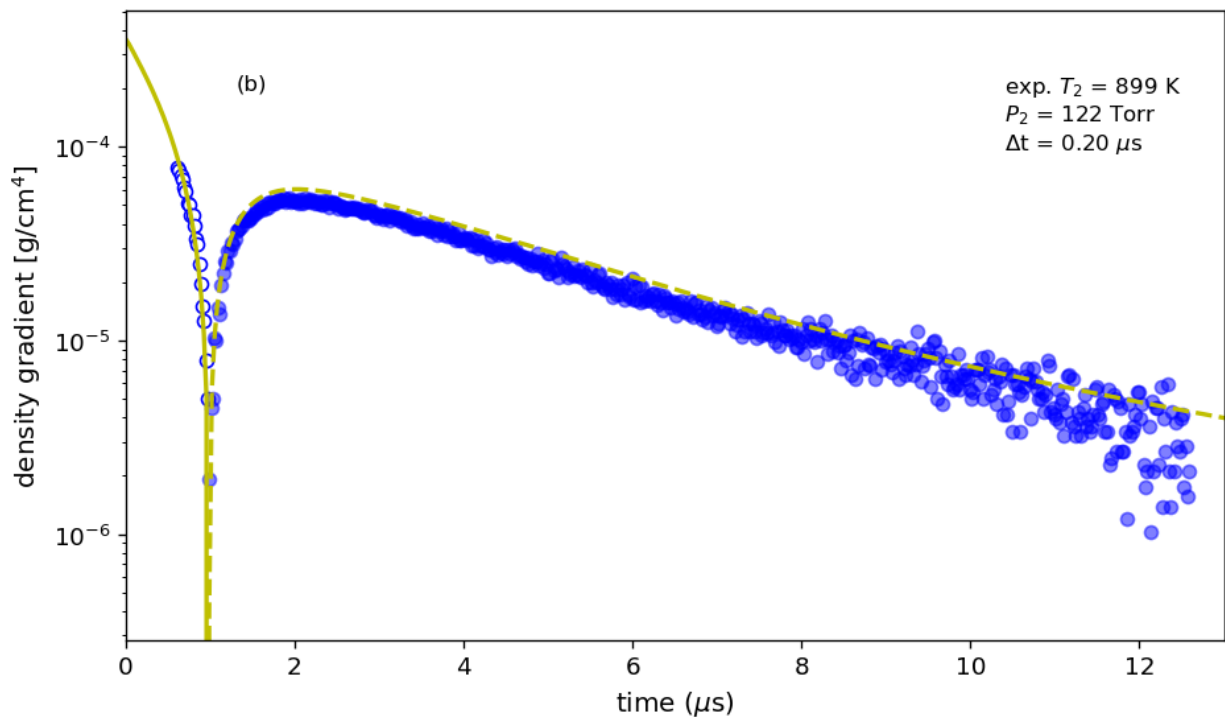
(a) Typical laser-schlieren raw signal
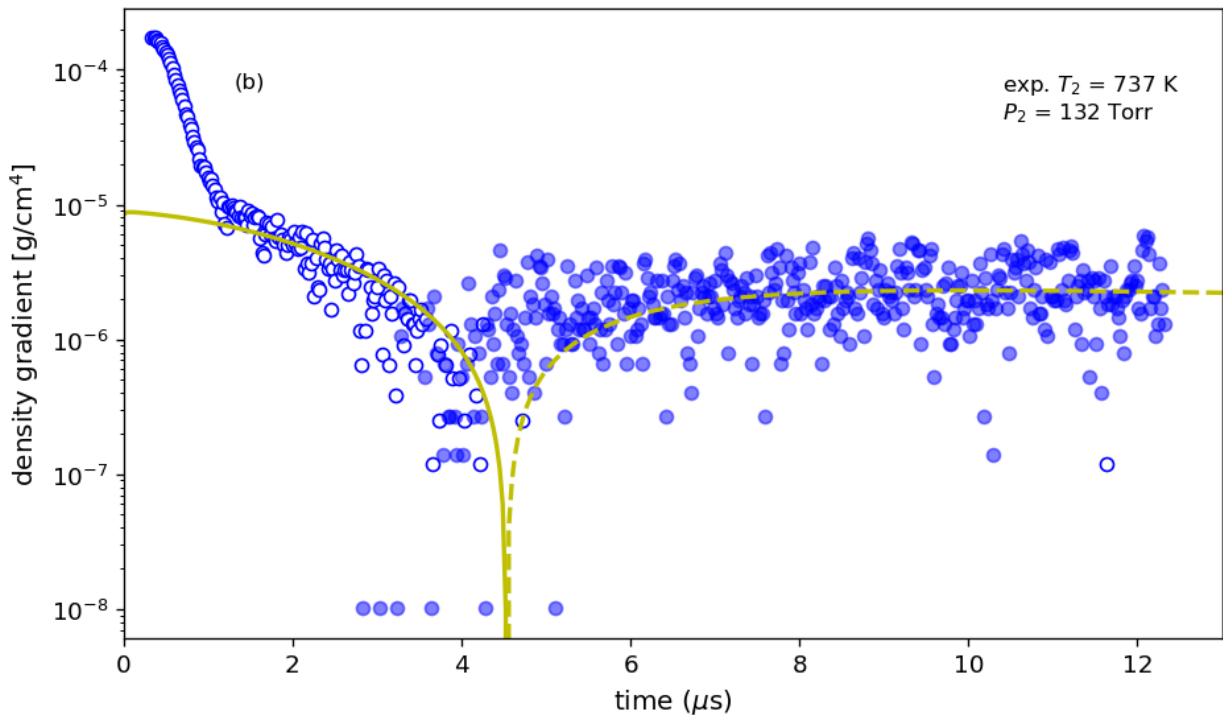
(b) Corresponding density gradient

Figure 5: Typical raw signal and density gradient for which location of time zero is accomplished by well-established methodology.[35]

(a) Multiply-peaked raw laser-schlieren signal

(b) Corresponding density gradient

Figure 6: A multiply-peaked raw signal still produces a measurable density gradient, but makes location of time zero uncertain and frequently requires manual time-shifting.

As may be seen from the density gradient corresponding to Figure 6a, Figure 6b, the existence of a multiple peaks in the raw signal does not prevent measurement of the density gradient behind the incident shock, but it does make determination of t_0 more difficult. For shocks with a double peak, the standard procedure to determine t_0 was not always robust; the resulting model predictions would be offset from but otherwise parallel to the experimental data. Accordingly, these shocks required a manual adjust to t_0, or a time-shift Δt.

In order to determine the necessary time shift, the reference model was run for a given experiment. In some instances, the predicted density gradient has the correct slope and curvature but is offset from the measured gradient. In those cases, the Δt was applied that resulted in correct alignment. This process was iterated, so as to avoid introducing any bias in the process.

The issue of time-shifting data for laser schlieren is not restricted to signals with double peaks, but rather can be a general consequence of the high time resolution of the method. A physical interpretation of Δt is the incubation period required for vibrational excitation of the molecule from the initial state to the post-shocked state. Incubation delays in LS experiments may require time shifting, particularly at low pressures,[81,94] with values typically in the range of 0.3 - 0.5 μs, e.g. Ref. 95. This observation is consistent with later work by Kiefer and Shah[96] in which the zero was shifted in all experiments by 0.2 μs to account for model simulations running parallel to the data. For benzene and fluorobenzene, incubation periods greater than 1 μs have been reported.[35,97]

For the present work, the time delay was no greater than 1 μs. For all density gradients where a time-shift was applied, the value is printed on the density gradient plot. A complete set of density gradient plots with results of the final model simulations overlaid is included in the Supplemental Material.

Minor uncertainty in t_0 is not unique to the LS diagnostic but is present in all shock tube measurements. However, other shock tube techniques, such as ignition delay times or laser absorption spectroscopy,[98] typically involve longer time scales and thus are less sensitive to

small uncertainty in t_0. For a broader discussion on the issues and consequences of time-shifting in chemical kinetics, the reader is referred to the analysis of Dryer and coworkers (where the time shift typically accounts for mixing effects, rather than post-shock vibrational excitation).[99]

Alternative chemistry to current model

In order to demonstrate the effect of different chemical kinetic submechanisms on the modeled density gradient, we consider alternative expressions for four of the reactions in Table 1. Reactions 11, 19, 24, and 26 were modified by Annesley et al. as part of their analysis on nitromethane pyrolysis.[67] Because the density gradient is sensitive to these reactions, it is worth considering the effect of uncertainties in secondary reactions on the modeled density gradients.
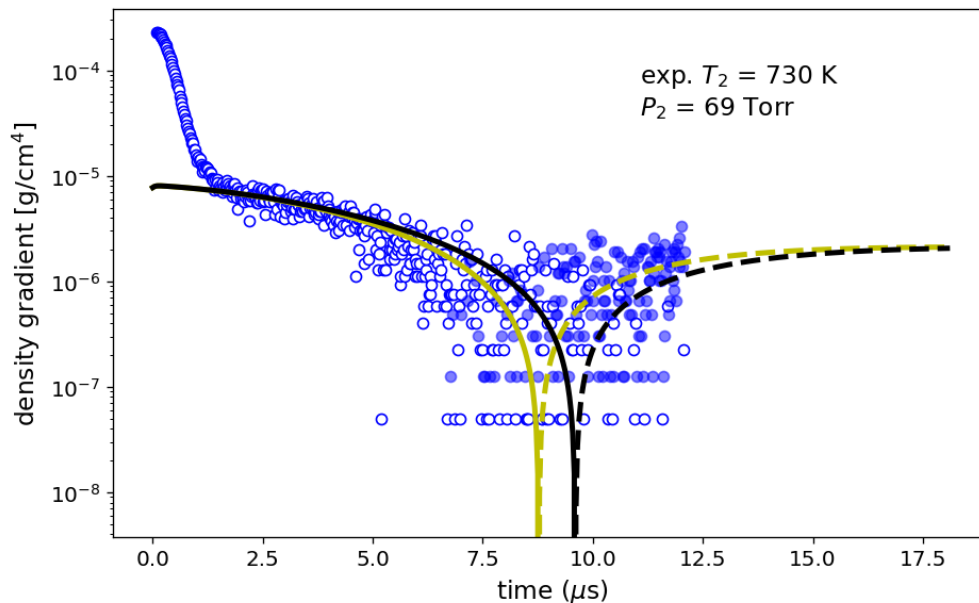

Figure 7: Effect of differing rates from Annesley et al. (black) as modification to Figure 2.
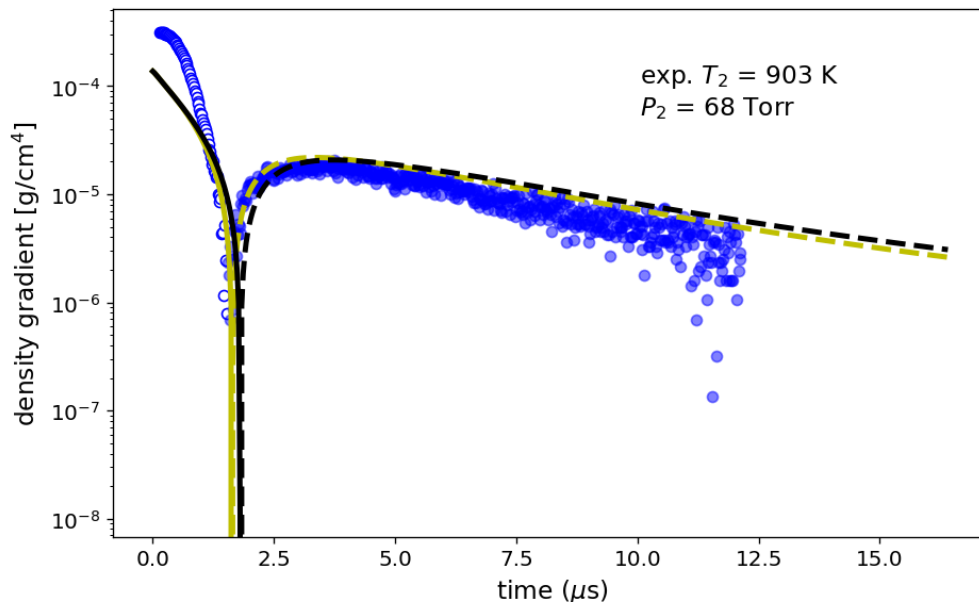
Figure 8: Effect of differing rates from Annesley et al. (black) as modification to Figure 3. [67]

Table 2: Reactions updated from the current mechanism by the work of Annesley et al. contributing to observed density gradients depicted in Figures 7 and 8. For pressure-dependent reactions, the high-pressure limit is presented.

Number	Reaction	A^a	n^a	$E_a{}^a$	k^a (800 K)	Ref.
11	$CH_3 + CH_3O \rightleftharpoons CH_2O + CH_4$	2.41e+13	0.0	0	2.41e+13	78
19	$CH_3 + NO_2 \rightleftharpoons CH_3O + NO$	1.10e+13	0.0	0	1.10e+13	87, 88
24	CH_3NO_2 (+M) $\rightleftharpoons CH_3 + NO_2$ (+M)	1.80e+16	0.0	58500	1.87e+0	87, 93
26	$CH_3NO_2 + H \rightleftharpoons CH_2NO_2 + H_2$	4.90e+13	0.0	9220	1.48e+11	100
11A	$CH_3 + CH_3O \rightleftharpoons CH_2O + CH_4$	7.50e+15	-1.0	501	6.84e+13	67
19A	$CH_3 + NO_2 \rightleftharpoons CH_3O + NO$	4.00e+13	-0.2	0	1.05e+13	67
24A	$CH_3NO_2 \rightleftharpoons CH_3 + NO_2$	5.22e+21	-1.56	61526	2.40e+0	67
26A	$CH_3NO_2 + H \rightleftharpoons CH_2NO_2 + H_2$	2.50e+2	3.50	5200	1.37e+11	67

^{a} Modified Arrhenius format, $k = A \left(T/T_0\right)^n \exp\left(-E_a/RT\right)$. Units: cm, s, K, mole, calorie.
$$T_0 = 1 \text{ K.}$$

As can be seen from Figure 7, the different submechanism shifts the time at which the density gradient changes sign by ~ 1 μs. At higher temperatures, Figure 8, the difference in model predictions is barely distinguishable. In both cases, the effect of the submechanism on the interpretation of the initial dissociation is within the stated uncertainty of the method.

Roaming

In the thermal decomposition of nitromethane, the departing NO_2 can undergo a roaming radical reaction and reattach to form methyl nitrite, CH_3ONO, which promptly dissociates to methoxy + nitric oxide. According to the combined experimental and theoretical analysis of Annesley et al., the branching fraction of this roaming pathway is likely between 10-15%.[67] For iPN, the analogous roaming pathway would form isopropylperoxy nitrite, $CH_3CH(OONO)CH_3$, which would promptly dissociate to isopropylperoxy + nitric oxide. This roaming pathway is unlikely to play a role in the thermal decomposition of iPN (or indeed most alkyl nitrates). On the CH_3NO_2 potential energy surface, the CH_3O + NO product channel is below the CH_3 + NO_2 asymptote by 16 kcal/mol, and thus prompt dissociation hot nitromethane is possible. On the $C_3H_7NO_3$ potential energy surface, in contrast, the $CH_3CH(OO)CH_3$ + NO product channel is above the $CH_3CH(O)CH_3$ + NO_2 asymptote by 11.4 kcal/mol, so any potential roaming intermediate that would have sufficient energy to dissociate to $CH_3CH(OO)CH_3$ + NO would be more likely to continue the dissociation towards $CH_3CH(O)CH_3$ + NO_2 instead.

However, there is another roaming radical pathway that could be important in iPN decomposition. In principle, the departing NO_2 could re-orient itself, fall into the attractive basin of the secondary hydrogen, and undergo disproportionation to form acetone + nitrous acid, i.e. the same products as Reaction (R1b). This pathway would be entirely independent of the tight transition state depicted in Figure 1. The present theoretical analysis does not include a full treatment of roaming kinetics. Instead, we consider the possible effect of roaming on the modeled density gradient and use the measured density gradients to provide an upper bound for the roaming branching fraction. Because the roaming pathway is exothermic, $\Delta H_{rxn} = -25.5$ kcal/mol, any contribution from roaming to the total density gradient would result in a more rapid transition from positive to negative density gradient (i.e. shifting the downward spike in Figures 2 and 3 to the left). Accordingly, if the estimated branching fraction towards roaming is too large, then it will shift the modeled density

gradient outside the narrow band of measured density gradient.

The results of this analysis with a 20% branching fraction are presented in Figures 9 and 10 for the same conditions as Figures 2 and 3, respectively. From the analysis, it is clear that at lower temperatures, a roaming branching fraction of 20% would no longer adequately capture the profile, whereas a branching fraction of 10-15% would not be inconsistent with the data. A full theoretical treatment of roaming reactions for alkyl nitrates will be the subject of a separate, forthcoming work. Without this theory-informed constraint, a more accurate determination of the roaming branching fraction is not possible within the current experimental margin of error.
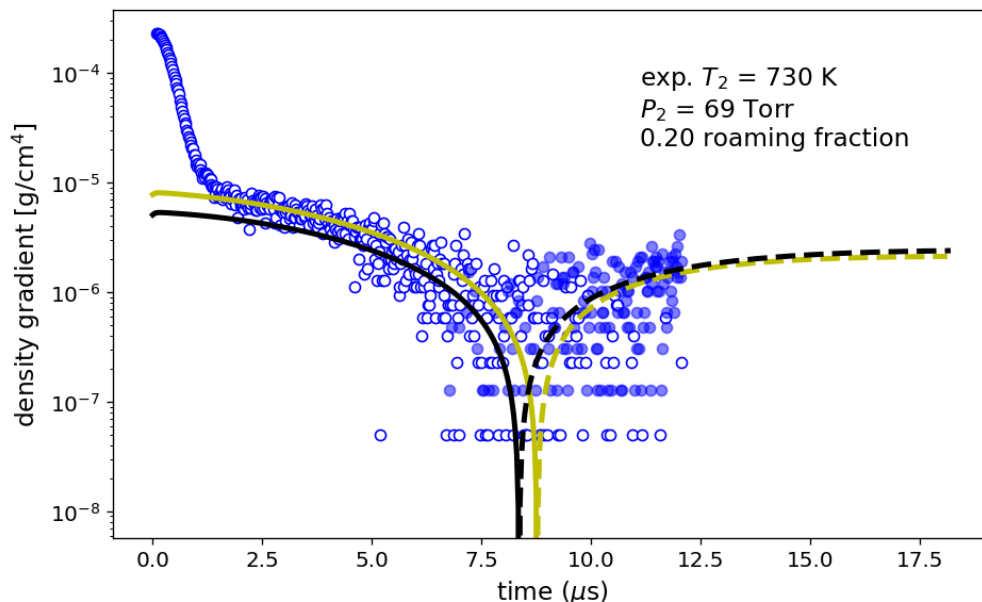

Figure 9: Effect of 20% roaming on model predictions (black) as modification to Figure 2. The roaming pathway produces an exothermic (negative) contribution to the density gradient, *cf.* Figure 1, which clearly alters the low-temperature signal.
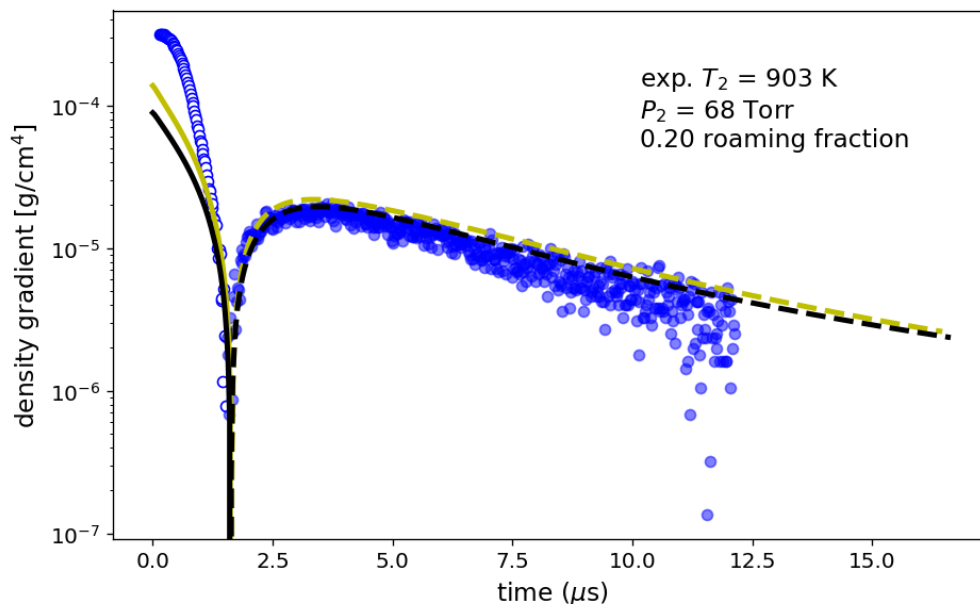
Figure 10: Effect of 20% roaming on model predictions (black) as modification to Figure 3. The effect on the density gradient signal owing to roaming is masked by the rapid dissociation of isopropyl nitrate and transition to exothermic secondary chemistry at high temperatures.

Summary

The decomposition of isopropyl nitrate was measured behind incident shock waves using laser schlieren densitometry in a new diaphragmless shock tube facility. Experiments were conducted over the range of 700 - 1000 K and at pressures of 71, 126, and 240 Torr. Electronic structure theory and RRKM Master Equation methods were used to predict the decomposition kinetics. Select RRKM/ME parameters were optimized in a novel procedure against the experimental data to provide an accurate prediction over a broader range of conditions. The measured dissociation rate constants are in excellent agreement with prior experimental studies. A new chemical kinetic mechanism was developed to model the radical-radical chemistry after the initial dissociation. A new shock tube module was developed for CAN-TERA, which allows for arbitrarily large mechanisms in the simulation of laser schlieren experiments. This new modeling capability allows for mechanism validation for the entire LS signal. The current data place an upper limit of 15% on the roaming reaction to form

acetone and HONO.

Acknowledgement

Supporting Information Available

The following files are available free of charge.

- Supplemental_ShockSummary.pdf: A complete list of shocks with experimental conditions, measured rate constant, and plots of density gradient and final model results

- Supplemental_Mechanism.cti: The chemical kinetic mechanism and thermodynamic data used to model the experiments including the final fit to the rate of isopropyl nitrate dissociation, formatted for use with CANTERA.

- Supplemental_ShockEquations.pdf: derivation of the shock equations and density gradient, as implemented in CANTERA.

- Supplemental_DensityGradients.zip: a directory containing the measured density gradients.

References

(1) Tanaka, S.; Ayala, F.; Keck, J. C.; B.Heywood, J. Two-stage ignition in HCCI combustion and HCCI control by fuels and additives. *Combustion and Flame* **2003**, *132*, 219–239.

(2) Splitter, D.; Reitz, R.; Hanson, R. High Efficiency, Low Emissions RCCI Combustion by Use of a Fuel Additive. *SAE International Journal of Fuels and Lubricants* **2010**, *3*, 742–756.

(3) Dempsey, A. B.; Walker, N. R.; Reitz, R. D. Effect of Cetane Improvers on Gasoline, Ethanol, and Methanol Reactivity and the Implications for RCCI Combustion. *SAE International Journal of Fuels and Lubrication* **2013**, *6*, 170–187.

(4) Splitter, D.; Wissink, M.; DelVescovo, D.; Reitz, R. D. RCCI Engine Operation Towards 60% Thermal Efficiency. SAE Technical Paper Series. 2013.

(5) Splitter, D. A.; Reitz, R. D. Fuel reactivity effects on the efficiency and operational window of dual-fuel compression ignition engines. *Fuel* **2014**, *118*, 163–175.

(6) Reitz, R. D.; Duraisamy, G. Review of high efficiency and clean reactivity controlled compression ignition (RCCI) combustion in internal combustion engines. *Progress in Energy and Combustion Science* **2015**, *46*, 12–71.

(7) Hiskey, M. A.; Brower, K. R.; Oxley, J. C. Thermal Decomposition of Nitrate Esters. *The Journal of Physical Chemistry* **1991**, *95*, 3955–3960.

(8) Oxley, J. C.; Smith, J. L.; Rogers, E.; Ye, W.; Aradi, A. A.; Henly, T. J. Fuel Combustion Additives: A Study of Their Thermal Stabilities and Decomposition Pathways. *Energy & Fuels* **2000**, *14*, 1252–1264.

(9) Oxley, J. C.; Smith, J. L.; Rogers, E.; Ye, W.; Aradi, A. A.; Henly, T. J. Heat-Release Behavior of Fuel Combustion Additives. *Energy & Fuels* **2001**, *15*, 1194–1199.

(10) Zeng, X.-L.; Chen, W.-H.; Liu, J.-C.; Kan, J.-L. A theoretical study of five nitrates: Electronic structure and bond dissociation energies. *Journal of Molecular Structure: THEOCHEM* **2007**, *810*, 47–51.

(11) Zaslonko, I. S.; Smirnov, V. N.; Tereza, A. M. High-Temperature Decomposition of Methyl, Ethyl, and Isopropyl Nitrates in Shock Waves. *Kinetics and Catalysis* **1993**, *34*, 531–538.

(12) Toland, A.; Simmie, J. M. Ignition of alkyl nitrate/oxygen/argon mixtures in shock waves and comparisons with alkanes and amines. *Combustion and Flame* **2003**, *132*, 556–564.

(13) Hartmann, M.; Tian, K.; Hofrath, C.; Fikri, M.; Schubert, A.; Schießl, R.; Starke, R.; Atakan, B.; Schulz, C.; Maas, U. et al. Experiments and modeling of ignition delay times, flame structure and intermediate species of EHN-doped stoichiometric n-heptane/air combustion. *Proceedings of the Combustion Institute* **2009**, *32*, 197–204.

(14) Beeley, P.; Griffiths, J.; Gray, P. Rapid compression studies on spontaneous ignition of isopropyl nitrate art I: Nonexplosive decomposition, explosive oxidation and conditions for safe handling. *Combustion and Flame* **1980**, *39*, 255–268.

(15) Beeley, P.; Griffiths, J.; Gray, P. Rapid compression studies on spontaneous ignition of isopropyl nitrate Part II: Rapid sampling, intermediate stages and reaction mechanisms. *Combustion and Flame* **1980**, *39*, 269–281.

(16) Goldsborough, S.; Johnson, M.; Banyon, C.; Pitz, W.; McNenly, M. Experimental and modeling study of fuel interactions with an alkyl nitrate cetane enhancer, 2-ethyl-hexyl nitrate. *Proceedings of the Combustion Institute* **2015**, *35*, 571–579.

(17) Bornemann, H.; Scheidt, F.; Sander, W. Thermal decomposition of 2-ethylhexyl nitrate (2-EHN). *International Journal of Chemical Kinetics* **2001**, *34*, 34–38.

(18) Stein, Y.; Yetter, R. A.; Dryer, F. L.; Aradi, A. The Autoignition Behavior of Surrogate Diesel Fuel Mixtures and the Chemical Effects of 2-Ethylhexyl Nitrate (2-EHN) Cetane Improver. *SAE Transactions* **1999**, *108*, 1029–1045.

(19) Romanias, M. N.; Morin, J.; Bedjanian, Y. Experimental Study of the Reaction of Isopropyl Nitrate with OH Radicals: Kinetics and Products. *International Journal of Chemical Kinetics* **2014**, *47*, 42–49.

(20) Morin, J.; Bedjanian, Y. Thermal Decomposition of Isopropyl Nitrate: Kinetics and Products. *The Journal of Physical Chemistry A* **2016**, *120*, 8037–8043.

(21) Morin, J.; Bedjanian, Y.; Romanias, M. N. Kinetics and Products of the Reactions of Ethyl and n-Propyl Nitrates with OH Radicals. *International Journal of Chemical Kinetics* **2016**, *48*, 822–829.

(22) Bedjanian, Y.; Morin, J.; Romanias, M. N. Kinetics of the reactions of OH radicals with n-butyl, isobutyl, n-pentyl and 3-methyl-1-butyl nitrates. *Atmospheric Environment* **2017**, *155*, 29–34.

(23) Appin, A.; Chariton, J.; Todes, O. The thermal decomposition and explosion of methyl nitrate vapour. *Acta Physicochem* **1936**, *5*, 655 – 678.

(24) Goodman, H.; Gray, P.; Jones, D. Self-heating during the spontaneous ignition of methyl nitrate vapor. *Combustion and Flame* **1972**, *19*, 157–169.

(25) Griffiths, J.; Gilligan, M.; Gray, P. Pyrolysis of isopropyl nitrate. I. Decomposition at low temperatures and pressures. *Combustion and Flame* **1975**, *24*, 11–19.

(26) Griffiths, J.; Gilligan, M.; Gray, P. Pyrolysis of isopropyl nitrate. II. Decomposition at high temperatures and pressures. *Combustion and Flame* **1976**, *26*, 385–393.

(27) Fifer, R. A. High temperature pyrolysis of methyl (and ethyl) nitrate. *Symposium (International) on Combustion* **1979**, *17*, 587–599.

(28) Hansson, T.; Pettersson, J. B. C.; Holmlid, L. A molecular beam mass-spectrometric study of isopropyl nitrate pyrolysis reactions at short residence times and temperatures up to 700 K. *Journal of the Chemical Society, Faraday Transactions 2* **1989**, *85*, 1413.

(29) Jones, D. E. G.; Feng, H. T.; Augsten, R. A.; Fouchard, R. C. *Journal of Thermal Analysis and Calorimetry* **1999**, *55*, 9–19.

(30) Gong, X.; Xiao, H. Studies on the molecular structures, vibrational spectra and thermodynamic properties of organic nitrates using density functional theory and ab initio methods. *Journal of Molecular Structure: THEOCHEM* **2001**, *572*, 213–221.

(31) Roos, B. D.; Brill, T. B. Thermal decomposition of energetic materials 82. Correlations of gaseous products with the composition of aliphatic nitrate esters. *Combustion and Flame* **2002**, *128*, 181–190.

(32) Lohr, L. L.; Barker, J. R.; Shroll, R. M. Modeling the Organic Nitrate Yields in the Reaction of Alkyl Peroxy Radicals with Nitric Oxide. 1. Electronic Structure Calculations and Thermochemistry. *The Journal of Physical Chemistry A* **2003**, *107*, 7429–7433.

(33) Miller, M. S.; Anderson, W. R. Burning-Rate Predictor for Multi-Ingredient Propellants: Nitrate-Ester Propellants. *Journal of Propulsion and Power* **2004**, *20*, 440–454.

(34) Arenas, J. F.; Avila, F. J.; Otero, J. C.; Peláez, D.; Soto, J. Approach to the Atmospheric Chemistry of Methyl Nitrate and Methylperoxy Nitrite. Chemical Mechanisms of Their Formation and Decomposition Reactions in the Gas Phase. *The Journal of Physical Chemistry A* **2008**, *112*, 249–255.

(35) Kiefer, J. H. In *Shock Waves in Chemistry*; Lifshitz, A., Ed.; Marcel Dekker, Inc., 1981; Chapter 5, pp 219–277.

(36) Kiefer, J. H.; Al-Alami, M. Z.; Hajduk, J.-C. Physical optics of the laser-schlieren shock tube technique. *Applied Optics* **1981**, *20*, 221.

(37) Kiefer, J. H. Refractive index change and curvature in shock waves by angled beam refraction. *Review of Scientific Instruments* **1981**, *52*, 1392.

(38) Zádor, J.; Miller, J. A. Unimolecular dissociation of hydroxypropyl and propoxy radicals. *Proceedings of the Combustion Institute* **2013**, *34*, 519–526.

(39) Randazzo, J. B.; Fuller, M. E.; Goldsmith, C. F.; Tranter, R. S. Thermal dissociation of alkyl nitrites and recombination of alkyl radicals. *Proceedings of the Combustion Institute* **2019**, *37*, 703–710.

(40) Fuller, M. E.; Skowron, M.; Tranter, R. S.; Goldsmith, C. F. A modular, multi-diagnostic, automated shock tube for gas-phase chemistry. *Review of Scientific Instruments (in press)* **2019**,

(41) Tranter, R. S.; Giri, B. R. A diaphragmless shock tube for high temperature kinetic studies. *Review of Scientific Instruments* **2008**, *79*, 094103.

(42) Randazzo, J. B.; Tranter, R. S. Note: An improved driver section for a diaphragmless shock tube. *Review of Scientific Instruments* **2015**, *86*, 016117.

(43) Tranter, R. S.; Lynch, P. T.; Randazzo, J. B.; Lockhart, J. P. A.; Chen, X.; Goldsmith, C. F. High temperature pyrolysis of 2-methyl furan. *Physical Chemistry Chemical Physics* **2018**, *20*, 10826–10837.

(44) Kiefer, J. H.; Lutz, R. W. Vibrational Relaxation of Deuterium by a Quantitative Schlieren Method. *The Journal of Chemical Physics* **1966**, *44*, 658–667.

(45) Kiefer, J. H.; Lutz, R. W. Vibrational Relaxation of Hydrogen. *The Journal of Chemical Physics* **1966**, *44*, 668–672.

(46) Gardiner, W.; Hidaka, Y.; Tanzawa, T. Refractivity of combustion gases. *Combustion and Flame* **1981**, *40*, 213–219.

(47) ACD/Labs, Percepta Platform. www.acdlabs.com/products/percepta/predictors.php, `https://www.acdlabs.com/products/percepta/predictors.php`.

(48) Royal Society of Chemistry, ChemSpider. www.chemspider.com/, `http://www.chemspider.com/`.

(49) Peverati, R.; Truhlar, D. G. Improving the Accuracy of Hybrid Meta-GGA Density Functionals by Range Separation. *Journal of Physical Chemistry Letters* **2011**, *2*, 2810–2817.

(50) Adler, T. B.; Knizia, G.; Werner, H.-J. A simple and efficient CCSD(T)-F12 approximation. *The Journal of Chemical Physics* **2007**, *127*, 221106.

(51) Adler, T. B.; Werner, H.-J.; Manby, F. R. Local explicitly correlated second-order perturbation theory for the accurate treatment of large molecules. *The Journal of Chemical Physics* **2009**, *130*, 054106.

(52) Knizia, G.; Adler, T. B.; Werner, H.-J. Simplified CCSD(T)-F12 methods: Theory and benchmarks. *The Journal of Chemical Physics* **2009**, *130*, 054104.

(53) Georgievskii, Y.; Miller, J. A.; Burke, M. P.; Klippenstein, S. J. Reformulation and solution of the master equation for multiple-well chemical reactions. *The Journal of Physical Chemistry A* **2013**, *117*, 12146–12154.

(54) Georgievskii, Y.; Klippenstein, S. J. MESS: Master Equation System Solver 2016.3.23. `http://tcg.cse.anl.gov/papr/codes/mess.html/`.

(55) Georgievskii, Y.; Miller, J. A.; Burke, M. P.; Klippenstein, S. J. PAPR: Predictive Automated Phenomenological Rates v1. `http://tcg.cse.anl.gov/papr/`.

(56) Hirschfelder, J. O.; Wigner, E. Some Quantum-Mechanical Considerations in the Theory of Reactions Involving an Activation Energy. *The Journal of Chemical Physics* **1939**, *7*, 616.

(57) Miller, W. H. Unified Statistical Model for "Complex" and "Direct" Reaction Mechanisms. *The Journal of Chemical Physics* **1976**, *65*, 2216–2223.

(58) Chesnavich, W. J.; Bass, L.; Su, T.; Bowers, M. T. Multiple Transition States in Unimolecular Reactions: A Transition State Switching Model. Application to the $C_4H_8 + \cdot$ System. *The Journal of Chemical Physics* **1981**, *74*, 2228–2246.

(59) Chen, X.; Fuller, M. E.; Goldsmith, C. F. Decomposition Kinetics for HONO and HNO_2. *Reaction Chemistry & Engineering* **2019**, *4*, 323–333.

(60) Chai, J.; Goldsmith, C. F. Rate coefficients for fuel $+ NO_2$: Predictive kinetics for HONO and HNO_2 formation. *Proceedings of the Combustion Institute* **2017**, *36*, 617–626.

(61) Fuller, M. E.; Goldsmith, C. F. On the Modeling Implications of Treating HONO and HNO_2 as Distinct Chemical Species in Combustion. *Proceedings of the Combustion Institute* **2019**, *37*, 695–702.

(62) Grimme, S. Semiempirical hybrid density functional with perturbative second-order correlation. *Journal of Chemical Physics* **2006**, *124*, 034108.

(63) Grimme, S.; Antony, J.; Ehrlich, S.; Krieg, H. A consistent and accurate ab initio parametrization of density functional dispersion correction (DFT-D) for the 94 elements H-Pu. *Journal of Chemical Physics* **2010**, *132*, 154104.

(64) Goerigk, L.; Grimme, S. A thorough benchmark of density functional methods for general main group thermochemistry, kinetics, and noncovalent interactions. *Physical Chemistry Chemical Physics* **2011**, *13*, 6670.

(65) Frisch, M. J.; Trucks, G. W.; Schlegel, H. B.; Scuseria, G. E.; Robb, M. A.; Cheese-man, J. R.; Scalmani, G.; Barone, V.; Petersson, G. A.; Nakatsuji, H. et al. Gaussian 09 Revision D.01. 2013; Gaussian Inc. Wallingford CT.

(66) Werner, H.-J.; Knowles, P. J.; Knizia, G.; Manby, F. R.; Schütz, M.; Celani, P.; Györffy, W.; Kats, D.; Korona, T.; Lindh, R. et al. MOLPRO, version 2015.1, a package of ab initio programs. 2015; see http://www.molpro.net.

(67) Annesley, C. J.; Randazzo, J. B.; Klippenstein, S. J.; Harding, L. B.; Jasper, A. W.; Georgievskii, Y.; Ruscic, B.; Tranter, R. S. Thermal Dissociation and Roaming Isomer-ization of Nitromethane: Experiment and Theory. *The Journal of Physical Chemistry A* **2015**, *119*, 7872–7893.

(68) Ghigo, G.; Roos, B. O.; Malmqvist, P.-Å. A modified definition of the zeroth-order Hamiltonian in multiconfigurational perturbation theory (CASPT2). *Chemical Physics Letters* **2004**, *396*, 142–149.

(69) Burke, M. P.; Klippenstein, S. J.; Harding, L. B. A quantitative explanation for the apparent anomalous temperature dependence of $OH+HO_2=H_2O+O_2$ through multi-scale modeling. *Proceedings of the Combustion Institute* **2013**, *34*, 547 – 555.

(70) Burke, M. P.; Goldsmith, C. F.; Klippenstein, S. J.; Welz, O.; Huang, H.; Antonov, I. O.; Savee, J. D.; Osborn, D. L.; Zádor, J.; Taatjes, C. A. et al. Mul-tiscale Informatics for Low-Temperature Propane Oxidation: Further Complexities in Studies of Complex Reactions. *The Journal of Physical Chemistry A* **2015**, *119*, 7095–7115.

(71) Welz, O.; Burke, M. P.; Antonov, I. O.; Goldsmith, C. F.; Savee, J. D.; Osborn, D. L.; Taatjes, C. A.; Klippenstein, S. J.; Sheps, L. New Insights into Low-Temperature Ox-idation of Propane from Synchrotron Photoionization Mass Spectrometry and Multi-

scale Informatics Modeling. *The Journal of Physical Chemistry A* **2015**, *119*, 7116–7129.

(72) Burke, M. P. Harnessing the Combined Power of Theoretical and Experimental Data through Multiscale Informatics. *International Journal of Chemical Kinetics* **2016**, *48*, 212–235.

(73) Glarborg, P.; Miller, J. A.; Ruscic, B.; Klippenstein, S. J. Modeling nitrogen chemistry in combustion. *Progress in Energy and Combustion Science* **2018**, *67*, 31–68.

(74) Chen, X.; Goldsmith, C. F. Predictive kinetics for the thermal decomposition of RDX. *Proceedings of the Combustion Institute* **2019**, *37*, 3167 – 3173.

(75) Goos, E.; Burcat, A.; Ruscic, B. Ideal Gas Thermodynamic Data in Polynomial form for Combustion and Air Pollution Use. Available at http://garfield.chem.elte.hu/Burcat/burcat.html, `http://garfield.chem.elte.hu/Burcat/burcat.html`.

(76) Goodwin, D. G.; Speth, R. L.; Moffat, H. K.; Weber, B. W. Cantera: An Object-oriented Software Toolkit for Chemical Kinetics, Thermodynamics, and Transport Processes. `https://www.cantera.org`, 2018; Version 2.4.0.

(77) Kee, R. J.; Rupley, F. M.; Miller, J. A.; Coltrin, M. E.; Grcar, J. F.; Meeks, E.; Moffat, H. K.; Lutz, A. E.; Dixon-Lewis, G.; Smooke, M. D. et al. CHEMKIN Release 4.1.1. 2007.

(78) Tsang, W.; Hampson, R. F. Chemical Kinetic Data Base for Combustion Chemistry. Part I. Methane and Related Compounds. *Journal of Physical and Chemical Reference Data* **1986**, *15*, 1087–1279.

(79) Labbe, N. J.; Sivaramakrishnan*, R.; Goldsmith, C. F.; Georgievskii, Y.; Miller, J. A.; Klippenstein, S. J. Weakly Bound Free Radicals in Combustion: "Prompt" Dissocia-

tion of Formyl Radicals and Its Effect on Laminar Flame Speeds. *Journal of Physical Chemistry Letters* **2016**, *7*, 85–9.

(80) Labbe, N. J.; Sivaramakrishnan*, R.; Goldsmith, C. F.; Georgievskii, Y.; Miller, J. A.; Klippenstein, S. J. Ramifications of including non-equilibrium effects for HCO in flame chemistry. *Proceedings of the Combustion Institute* **2017**, *36*, 525–532.

(81) Yang, X.; Jasper, A. W.; Kiefer, J. H.; Tranter, R. S. The Dissociation of Diacetyl: A Shock Tube and Theoretical Study. *The Journal of Physical Chemistry A* **2009**, *113*, 8318–8326.

(82) Sivaramakrishnan, R.; Su, M.-C.; Michael, J. V.; Klippenstein, S. J.; Harding, L. B.; Ruscic, B. Shock Tube and Theoretical Studies on the Thermal Decomposition of Propane: Evidence for a Roaming Radical Channel. *The Journal of Physical Chemistry A* **2011**, *115*, 3366–3379.

(83) Vasudevan, V.; Davidson, D. F.; Hanson, R. K. Direct measurements of the reaction $OH + CH_2O \rightarrow HCO + H_2O$ at high temperatures. *International Journal of Chemical Kinetics* **2004**, *37*, 98–109.

(84) Taylor, P. H.; Yamada, T.; Marshall, P. The reaction of OH with acetaldehyde and deuterated acetaldehyde: Further insight into the reaction mechanism at both low and elevated temperatures. *International Journal of Chemical Kinetics* **2006**, *38*, 489–495.

(85) Dammeier, J.; Colberg, M.; Friedrichs, G. Wide temperature range (T = 295 K and 770–1305 K) study of the kinetics of the reactions HCO + NO and $HCO + NO_2$ using frequency modulation spectroscopy. *Physical Chemistry Chemical Physics* **2007**, *9*, 4177.

(86) Choi, Y. M.; Lin, M. C. Kinetics and mechanisms for reactions of HNO with CH3 and C6 H5 studied by quantum-chemical and statistical-theory calculations. *International Journal of Chemical Kinetics* **2005**, *37*, 261–274.

(87) Glarborg, P.; Bendtsen, A. B.; Miller, J. A. Nitromethane dissociation: Implications for the CH3 + NO2 reaction. *International Journal of Chemical Kinetics* **1999**, *31*, 591–602.

(88) Wollenhaupt, M.; Crowley, J. N. Kinetic Studies of the Reactions CH_3 + NO_2 → Products, $CH_3$3O + NO_2 → Products, and OH + $CH_3C(O)CH_3$ → $CH_3C(O)OH$ + CH_3, over a Range of Temperature and Pressure. *The Journal of Physical Chemistry A* **2000**, *104*, 6429–6438.

(89) He, Y.; Sanders, W. A.; Lin, M. C. Thermal decomposition of methyl nitrite: kinetic modeling of detailed product measurements by gas-liquid chromatography and Fourier-transform infrared spectroscopy. *The Journal of Physical Chemistry* **1988**, *92*, 5474–5481.

(90) Caralp, F.; Rayez, M.-T.; Forst, W.; Gomez, N.; Delcroix, B.; Fittschen, C.; Devolder, P. Kinetic and mechanistic study of the pressure and temperature dependence of the reaction CH_3O+NO. *Journal of the Chemical Society, Faraday Transactions* **1998**, *94*, 3321–3330.

(91) McCaulley, J.; Anderson, S.; Jeffries, J.; Kaufman, F. Kinetics of the reaction of CH3O with NO2. *Chemical Physics Letters* **1985**, *115*, 180–186.

(92) Doughty, A.; Barnes, F.; Bromly, J.; Haynes, B. The mutually sensitied oxidation of ethylene and NO: An experimental and kinetic modeling study. *Symposium (International) on Combustion* **1996**, *26*, 589–596.

(93) Glänzer, K.; Troe, J. Reactions of Alkyl Radicals in the Shock Wave-Induced Pyrolysis of Nitroalkanes. *Berichte der Bunsengesellschaft für physikalische Chemie* **1974**, *78*, 182–184.

(94) Yang, X.; Goldsmith, C. F.; S.Tranter, R. Decomposition and Vibrational Relaxation

in CH$_3$I and Self-reaction of CH$_3$ Radicals. *The Journal of Physical Chemistry A* **2009**, *113*, 8307–8317.

(95) Tranter, R. S.; Lynch, P. T.; Yang, X. Dissociation of dimethyl ether at high temperatures. *Proceedings of the Combustion Institute* **2013**, *34*, 591–598.

(96) Kiefer, J. H.; Shah, J. N. Unimolecular dissociation of cyclohexene at extremely high temperatures: behavior of the energy-transfer collision efficiency. *Journal of Physical Chemistry* **1987**, *91*, 3024–3030.

(97) Lynch, P. T.; Annesley, C. J.; Tranter, R. S. Dissociation of ortho-benzyne radicals in the high temperature fall-off regime. *Proceedings of the Combustion Institute* **2015**, *35*, 145 – 152.

(98) Hanson, R. K.; Davidson, D. F. Recent advances in laser absorption and shock tube methods for studies of combustion chemistry. *Progress in Energy and Combustion Science* **2014**, *44*, 103–114.

(99) Dryer, F. L.; Haas, F. M.; Santner, J.; Farouk, T. I.; Chaos, M. Interpreting chemical kinetics from complex reaction–advection–diffusion systems: Modeling of flow reactors and related experiments. *Progress in Energy and Combustion Science* **2014**, *44*, 19–39.

(100) Zhang, K.; Li, Y.; Yuan, T.; Cai, J.; Glarborg, P.; Qi, F. An experimental and kinetic modeling study of premixed nitromethane flames at low pressure. *Proceedings of the Combustion Institute* **2011**, *33*, 407–414.